The Astrophysical Journal, 898:113 (11pp), 2020 August 1 https://doi.org/10.3847/1538-4357/ab9b7e

Spectral Features in Field-aligned Solar Wind Turbulence from Parker Solar Probe Observations

L.-L. Zhao[1], G. P. Zank[1,2], L. Adhikari[1], M. Nakanotani[1], D. Telloni[3], and F. Carbone[4]
[1] Center for Space Plasma and Aeronomic Research (CSPAR), The University of Alabama in Huntsville, Huntsville, AL 35805, USA
[2] Department of Space Science, The University of Alabama in Huntsville, Huntsville, AL 35899, USA
[3] National Institute for Astrophysics Astrophysical Observatory of Torino Via Osservatorio 20, I-10025 Pino Torinese, Italy
[4] National Research Council—Institute of Atmospheric Pollution Research, C/o University of Calabria, I-87036 Rende, Italy
Received 2020 May 13; revised 2020 June 7; accepted 2020 June 9; published 2020 July 29

Abstract

Parker Solar Probe (PSP) observed a large variety of Alfvénic fluctuations in the fast and slow solar wind flow during its two perihelia. The properties of Alfvénic solar wind turbulence have been studied for decades in the near-Earth environment. A spectral index of $-5/3$ or -2 for magnetic field fluctuations has been observed using spacecraft measurements, which can be explained by turbulence theories of nearly incompressible magnetohydrodynamics (NI MHD) or critical balance. In this study, a rigorous search of field-aligned solar wind is applied to PSP measurements for the first time, which yields two events in the apparently slow solar wind. The parallel spectra of the magnetic fluctuations in the inertial range show a $k_{\parallel}^{-5/3}$ power law. Probability distributions of the magnetic field show that these events are not contaminated by intermittent structures, which, according to previous studies, are known to modify spectral properties. The results presented here are consistent with spectral predictions from NI MHD theory and further deepen our understanding of the Alfvénic solar wind turbulence near the Sun.

Unified Astronomy Thesaurus concepts: Solar wind (1534); Interplanetary turbulence (830); Spectral index (1553)

1. Introduction

Turbulent fluctuations are highly anisotropic in the solar wind due to the presence of a large-scale magnetic field (Matthaeus et al. 1990; Zank & Matthaeus 1992, 1993; Narita et al. 2010; Zank et al. 2017). The velocity and magnetic field fluctuations have a shorter correlation length in the direction perpendicular to the magnetic field than in the parallel direction, as revealed by the anisotropy of the correlation function of fluctuations (e.g., Matthaeus et al. 1990; Horbury et al. 2012). Differentiating between parallel and perpendicular fluctuations is key to understanding the nature of solar wind turbulence.

The theory of Alfvénic turbulence of Goldreich & Sridhar (1995) assumes that the turbulence is in a critically balanced state. A nonlinearity parameter is introduced as $\zeta_\lambda \sim \frac{k_\perp v_\lambda}{k_\parallel v_A}$, where v_λ is the perturbation in the amplitude of velocity, v_A is the Alfvén velocity, $k_\parallel$ and $k_\perp$ are the parallel and perpendicular components of the wavevector. Like classical hydrodynamic turbulence, use of a constant energy transfer rate $\epsilon \sim v_\lambda^2/t_c \sim k_\perp v_\lambda^3$ where t_c is the cascade time, yields $v_\lambda^2 \sim k_\perp^{-2/3}\epsilon^{-2/3}$. Critical balance assumes that the parameter $\zeta_\lambda \sim 1$ and $v_A \sim v_L$ at the energy injection scale L, which then implies $\epsilon \sim \epsilon_{inj} \sim v_A^3/L$ and $t_c \sim k_\parallel^{-1} v_A^{-1}$. This is equivalent to equating the nonlinear eddy turnover timescale and the linear Alfvén timescale. It then follows that the scaling $k_\parallel \sim k_\perp^{2/3} L^{-1/3}$ holds for critically balanced turbulence. Therefore, the turbulence power spectrum is predicted to be anisotropic according to critical balance theory, i.e., $E(k_\perp) \propto k_\perp^{-5/3}$; $E(k_\parallel) \propto k_\parallel^{-2}$. We note that the critical balance theory of Goldreich & Sridhar (1995) is limited to the symmetric case where counter-propagating Alfvén waves have the same energy flux. However, an attempt to extend the critical balance conjecture to imbalanced turbulence was made by Lithwick et al. (2007), finding the same spectral scaling results of $k_\parallel^{-2}$ and $k_\perp^{-5/3}$.

On the other hand, the theory of nearly incompressible magnetohydrodynamics (NI MHD) suggests that solar wind turbulence in the plasma beta β (ratio between thermal pressure and magnetic pressure) $\sim$1 or $<$1 regime is a superposition or "2D + NI/slab" fluctuations, comprising a dominant 2D component and a minority NI/slab component that includes both slab and higher-order quasi-2D fluctuations (e.g., Zank & Matthaeus 1992, 1993; Hunana & Zank 2010; Adhikari et al. 2017; Zank et al. 2017, 2020). Pure 2D turbulence is characterized by a wavevector strictly perpendicular to the background magnetic field $\boldsymbol{k} \perp \boldsymbol{B}_0$, so that the turbulence power is zero except where $\boldsymbol{k} \perp \boldsymbol{B}_0$. For pure slab turbulence, the wavevector is strictly parallel to the background magnetic field $\boldsymbol{k} \| \boldsymbol{B}_0$. As shown by Zank et al. (2017), the NI MHD theory gives a perpendicular energy spectrum $E(k_\perp) \propto k_\perp^{-5/3}$ that is derived from the core 2D MHD equations. The parallel energy spectrum results from the NI corrections and does not necessarily follows a $k_\parallel^{-2}$ power law as critical balance theory suggests. Based on NI MHD theory, a companion paper by Zank et al. (2020) discusses the anisotropic turbulence power spectrum in detail. Their theoretical derivations show that the turbulence power spectrum in the inertial range can take different functional forms depending on the parameters related to different solar wind conditions. In the case of highly imbalanced turbulence with cross helicity $|\sigma_c| \sim 1$ or quasi-2D nonlinear interactions dominate (see their Figure 1), a Kolmogorov $k_\parallel^{-5/3}$ spectrum results.

Turbulence anisotropy in solar wind fluctuations has been studied using single and multi-spacecraft data (Matthaeus et al. 1990, 2005; Bieber et al. 1996; Milano et al. 2004; Dasso et al. 2005; Ruiz et al. 2011), which is an important factor for the scattering of energetic particles (Zhao et al. 2017; Fu et al. 2020).

From Taylor's hypothesis, the parallel or perpendicular spectrum can be constructed when the spacecraft velocity is parallel or perpendicular to the mean magnetic field. Based on a structure function technique, Tessein et al. (2009) find no dependence of the spectral index upon the orientation of the mean magnetic field. Note that the mean magnetic field direction in their study is estimated across the whole time interval, which is from 1 to 3 hr in duration, and thus corresponds to the field at the largest scale. However, Chen et al. (2011) find a parallel spectral index close to -2 by using multi-spacecraft measurements of Cluster and a locally averaged magnetic field instead of the global magnetic field. Horbury et al. (2008) identify a local mean magnetic field using a wavelet technique, and then calculate the angle between the local mean magnetic field and the flow direction θ_{VB}, allowing them to separate the data according to θ_{VB}. A spectral index of $-5/3$ is found for $\theta_{VB} \sim 90^0$, and -2 for $\theta_{VB} \sim 0^0$ using a single spacecraft data sets (Horbury et al. 2008; Podesta 2009), which is consistent with critical balance theory.

Wang et al. (2014) studied the influence of intermittency on the spectral anisotropy of solar wind turbulence by applying the wavelet technique to the Wind spacecraft measurements. They concluded that intermittency might affect the parallel fluctuation spectral index by pushing an intrinsic $-5/3$ scaling index toward to -2. The removal of intermittency makes the turbulence power spectrum less anisotropic. However, Yang et al. (2017) argue that intermittency affects only the perpendicular spectrum, and not the parallel spectrum. Wang et al. (2015) search for time intervals during which the magnetic field is nearly aligned with or perpendicular to the radial direction in the fast solar wind observed by Wind. A standard Fourier spectral analysis is done for each 6 minutes interval. They find the parallel spectral index is close to -2 for moderate-amplitude fluctuations, and close to $-5/3$ for small amplitude parallel fluctuations.

Recently, Telloni et al. (2019) extended the Wang et al. (2015) study to longer time intervals (>1 hr) to improve statistics. A thorough search is performed on 12 yr of Wind measurements and 17 highly magnetic field-aligned intervals with low magnetic compressibility were identified. Telloni et al. (2019) find that the unidirectionally propagating Alfvén waves in the fast solar wind exhibit a Kolmogorov-like $k_{\parallel}^{-5/3}$ spectrum during periods of strong turbulence. These features are inconsistent with critical balance theory, which requires counter-propagating Alfvén waves with equal energy. However, such a Kolmogorov-like $k_{\parallel}^{-5/3}$ spectrum can be described by the NI MHD turbulence model of Zank et al. (2017) since the dominant quasi-2D fluctuations couple with slab (counter-propagating Alfvén waves) turbulence in a "passive scalar" sense that leads to a $k_{\parallel}^{-5/3}$ spectrum (see Zank et al. 2020). It is also confirmed by Adhikari et al. (2019, 2020) that the nonlinear terms for the slab turbulence transport equation do not become zero in the presence of unidirectional Alfvén waves.

The NASA Parker Solar Probe (PSP; Fox et al. 2016) mission, launched on 2018 August 12, has now approached closer to the surface of the Sun than any other spacecraft, and has been providing information of the deeper inner heliosphere. Close to the Sun, the interplanetary magnetic field is more likely to be radial, as suggested by the simple spiral magnetic field model of Parker. Thus PSP provides an opportunity to explore the properties of the field-aligned solar wind turbulence. In this work, we present a precise analysis of the parallel magnetic field fluctuations in the inner heliosphere using PSP measurements. Data from PSP/Electromagnetic Fields Investigation (FIELDs; Bale et al. 2016) and PSP/Solar Wind Electrons Alphas and Protons (SWEAP; Kasper et al. 2016) instruments near PSP's first (2018 November 6, $\sim$35 $R_{\odot}$) and second perihelion (2019 April 4, $\sim$35 $R_{\odot}$) are analyzed.

The outline of this paper is as follows. Section 2 presents the search criteria for unidirectional parallel magnetic fluctuations, followed by a description of the Hilbert spectral analysis (HSA) technique used to study the spectral properties. Section 3 shows results from selected intervals with a corresponding discussion. Section 4 provides a summary and conclusions.

2. Analysis Technique

2.1. Data Selection

Following Wang et al. (2015) and Telloni et al. (2019), we search for intervals with rigorous parallel fluctuations $k_{\parallel}$ in PSP measurements. According to Taylor's hypothesis, the frequency spectrum can be converted to the wavenumber spectrum assuming $\omega = \boldsymbol{k} \cdot \boldsymbol{U}$, where $\boldsymbol{U} = \boldsymbol{U}_{\rm sw} - \boldsymbol{U}_{\rm sc}$ is the velocity of the solar wind flow relative to the spacecraft. Unlike measurements near 1 au, the spacecraft velocity of PSP could be large, especially near perihelion, so the spacecraft velocity should not be neglected. To find parallel fluctuations, we first calculate the angle between the magnetic field and flow velocity measured in the spacecraft frame θ_{VB} to determine the degree of field alignment. The following PSP plasma and magnetic field data were considered for the analysis: $\sim$0.22 s resolution plasma data in the spacecraft frame of reference (only available near perihelion), including solar wind bulk velocity and proton number density, measured by SWEAP SPC instrument, and downsampled magnetic field measurements with the same cadence of $\sim$0.22 s from the FIELDs magnetometer. We require that (i) the magnetic field and flow velocity are aligned within 20° (i.e., $0 \leqslant \theta_{VB} \leqslant 20°$ or $160° \leqslant \theta_{VB} \leqslant 180°$) for each data point in the interval, so that both the global and local mean magnetic field are oriented along the velocity field; (ii) the intervals should have a minimum length of at least 20 minutes ($\sim$5500 samples for the data with a cadence of $\sim$0.22 s) to ensure a continuous Alfvénic solar wind fluctuation; (iii) the intervals are characterized by low magnetic compressibility ($\leqslant$0.2), which is defined as the ratio between the power in the magnetic field magnitude fluctuations and the total power in the magnetic field fluctuations (Bavassano et al. 1982); (iv) the bad data or missing data in the interval should be no more than 20%. These criteria guarantee that the selected intervals are mostly populated by the undisturbed Alfvénic $k_{\parallel}$ fluctuations.

As noted by various studies (e.g., Bale et al. 2019; Kasper et al. 2019; Dudok de Wit et al. 2020; Horbury et al. 2020), PSP observed a number of magnetic switchback structures near the Sun. These structures are characterized by a deflection or even reversal in the magnetic field direction, accompanied by a deflection in flow velocity. The duration of magnetic switchbacks ranges from seconds to hours (e.g., Dudok de Wit et al. 2020; McManus et al. 2020). The prevailing magnetic switchbacks make the angle θ_{VB} jump up and down, although the mean of θ_{VB} is mostly parallel or anti-parallel depending on the polarity of the magnetic field. Therefore, the occurrence of purely parallel fluctuations satisfying the above four criteria is

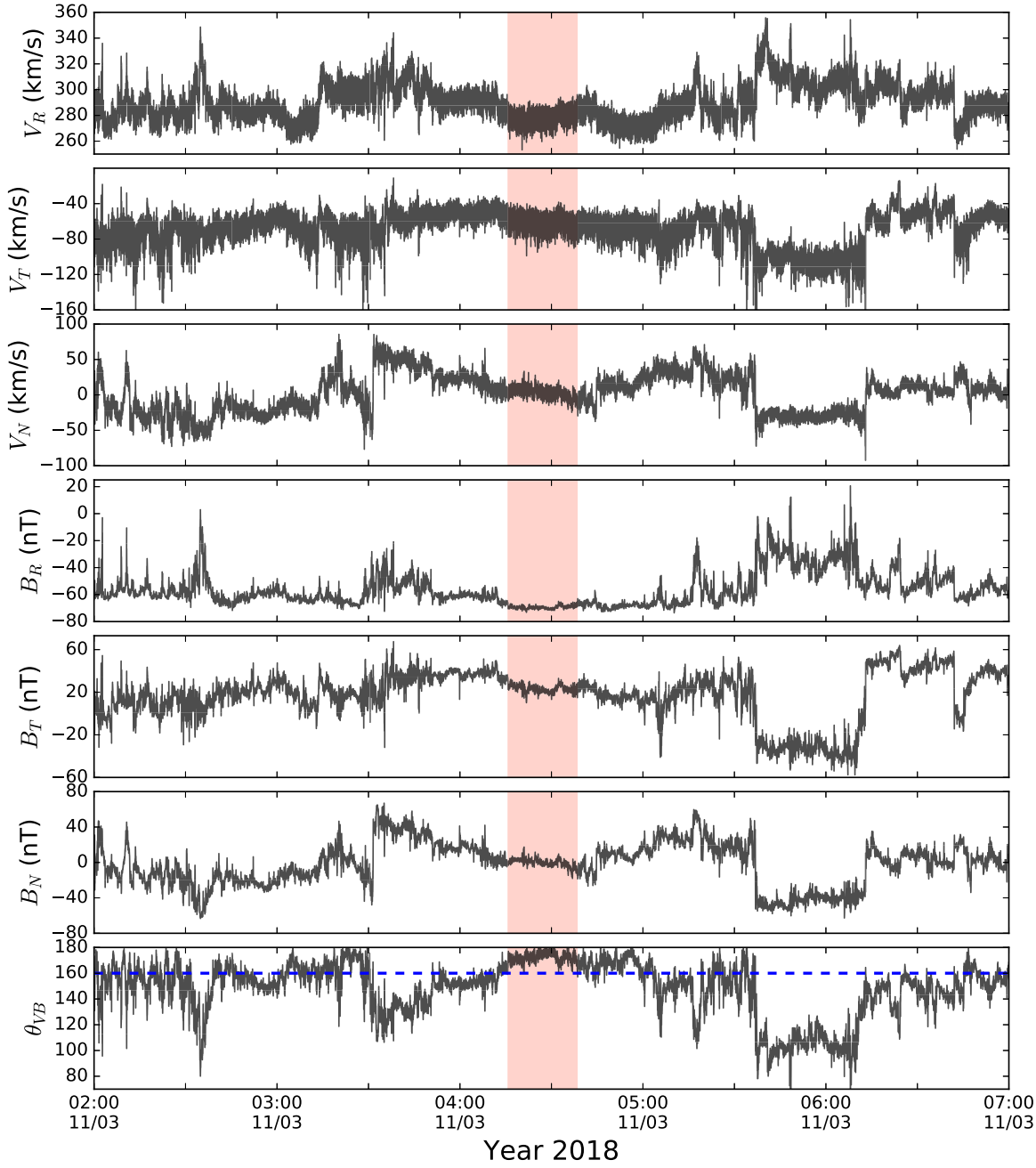

Figure 1. Solar wind parameters on 2018 November 3. Panels from top to bottom show the flow velocity components, magnetic field components, and the angle between magnetic field and velocity vectors. The shaded area shows the selected interval. The blue dashed line shows the threshold of θ_{VB} (160°) used in this study to select intervals.

Table 1
List of the Alfvénic Field-aligned Intervals

Date	Start Time (UT)	End Time (UT)	Duration (minutes)	Distance (au)	V_{sw} (km s^{-1})	$\lvert B\rvert$ (nT)	$\langle\theta_{VB}\rangle$ (°)	C_B
2018 Nov 3	04:15:35	04:38:36	23	0.194	251	73	172	0.04
2019 Apr 4	05:18:35	06:01:22	43	0.167	310	100	171	0.07

Note. V_{sw} is the averaged solar wind speed in the RTN frame, θ_{VB} is the angle between the local magnetic field and the flow direction, $|B|$ is the averaged magnetic field magnitude, and C_B is the averaged magnetic compressibility.

relatively rare, especially near perihelion. Telloni et al. (2019) also required that the intervals should be in the fast solar wind, but we do not impose this restriction on our study. The solar wind plasma observed by PSP during the first two orbits comprises mostly low-speed streams ($\leqslant$550 km s^{-1}). The high-speed streams have short periods, large fluctuations, and many

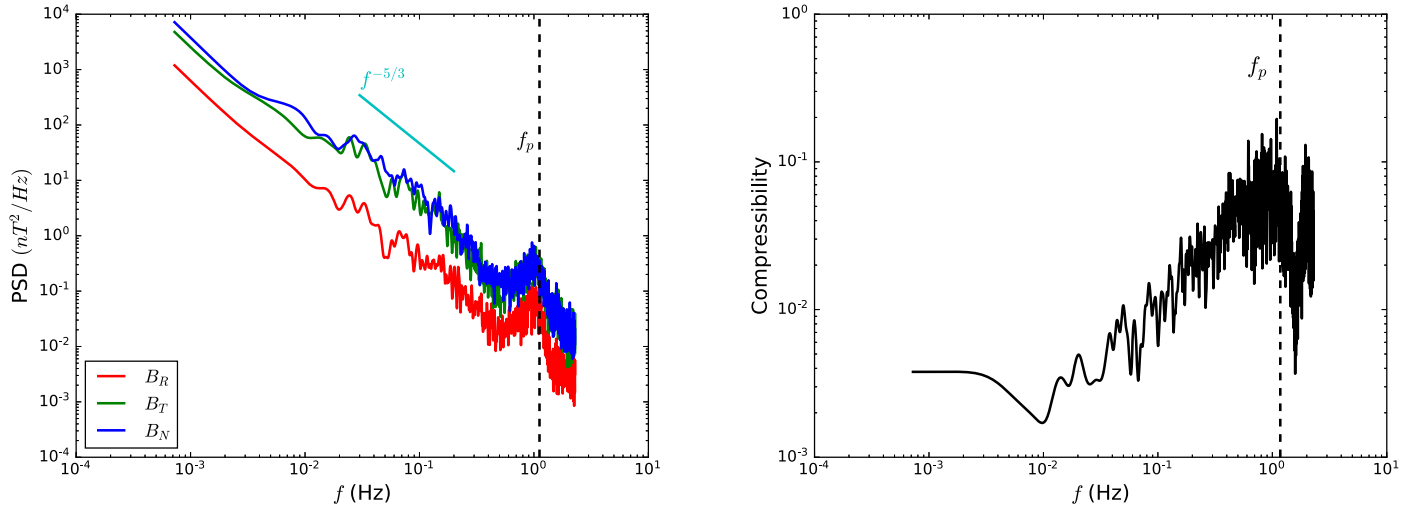

Figure 2. Left panel: the Fourier PSD of the B_R, B_T, and B_N components of the magnetic field for the selected interval shown in Figure 1. A Kolmogorov $f^{-5/3}$ spectrum is displayed as a reference. The dashed vertical line identifies the proton gyrofrequency $f_p = \frac{qB}{2\pi m_p}$. Right panel: the frequency-dependent magnetic compressibility, defined by the ratio of the power in the fluctuations of the magnetic field magnitude and the total power in the magnetic field fluctuations.

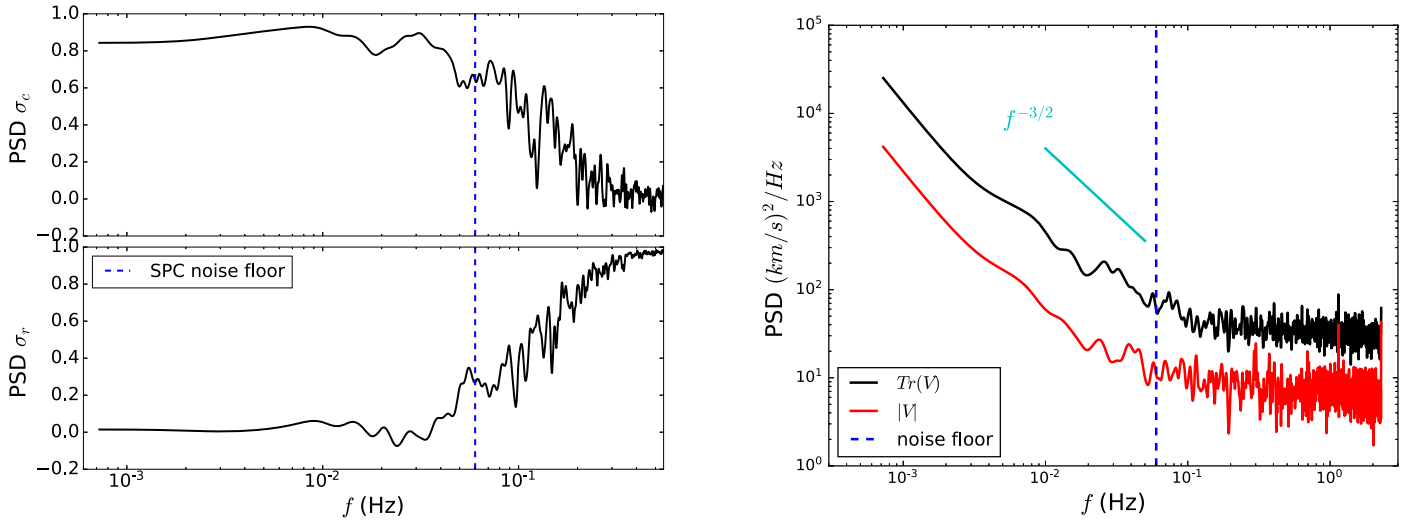

Figure 3. Left panel: Fourier power spectra of the normalized cross helicity σ_c and normalized residual energy σ_r for the interval selected in Figure 1. Right panel: the trace power spectrum (black curve) of velocity fluctuations and the spectrum of the velocity magnitude fluctuations (red curve). The spectra are analyzed for the ~5 Hz cadence plasma velocity data in a ~23 minutes interval. The blue vertical dashed line identifies the frequency at which the velocity spectrum begins to flatten and where noise may become important (Parashar et al. 2020).

switchbacks, which makes it difficult to find purely parallel fluctuation intervals.

2.2. Hilbert Spectral Analysis

Similar to Telloni et al. (2019), we use a HSA along with the standard Fourier spectral analysis. The HSA is based on the Hilbert–Huang transformation (HHT), and has the advantage of analyzing nonlinear and non-stationary data without on a priori base (Huang et al. 2008, 2011). Recently, HSA has been applied successfully to study the properties of solar wind turbulence in the inertial and kinetic ranges (e.g., Carbone et al. 2018; Telloni et al. 2019). The first step is to decompose the signal (each component of the magnetic field B_R, B_T, and B_N in this work) into a finite number of intrinsic mode functions $\phi_j(t)$ (IMFs), where each IMF $\phi_j(t)$ ($j = 1, 2, ..., k$) satisfies the conditions (i) the number of extrema and zero crossings differ by at most 1; (ii) at any point, the mean value of the envelope defined by the local maxima and the envelope defined by the local minima is 0. Therefore, $B_{i=R,T,N} = \sum_{j=1}^{k} \phi_j(t) + r(t)$, and $r(t)$ is a residual that describes the mean variation. The procedure of obtaining IMFs from an arbitrary time-series signal is known as empirical mode decomposition (EMD), which is based on a sifting process. The IMFs thus obtained are narrow banded. The effects of pseudo-harmonics or artifacts in the vicinity of sharp data transitions can be eliminated by using the EMD technique. Once the IMFs are obtained, the Hilbert transform $\mathcal{H}$ can be applied to each IMF. The analytic signal with the HHT is then defined as

$$Z_j(t) = \phi_j(t) + i\tilde{\phi}_j(t) = A_j(t)e^{i\theta_j(t)},$$

where

$$\tilde{\phi}_j(t) = \mathcal{H}(\phi_j(t)) = \frac{1}{\pi} PV \int_{-\infty}^{\infty} \frac{\phi_j(t)}{t-\tau} d\tau,$$

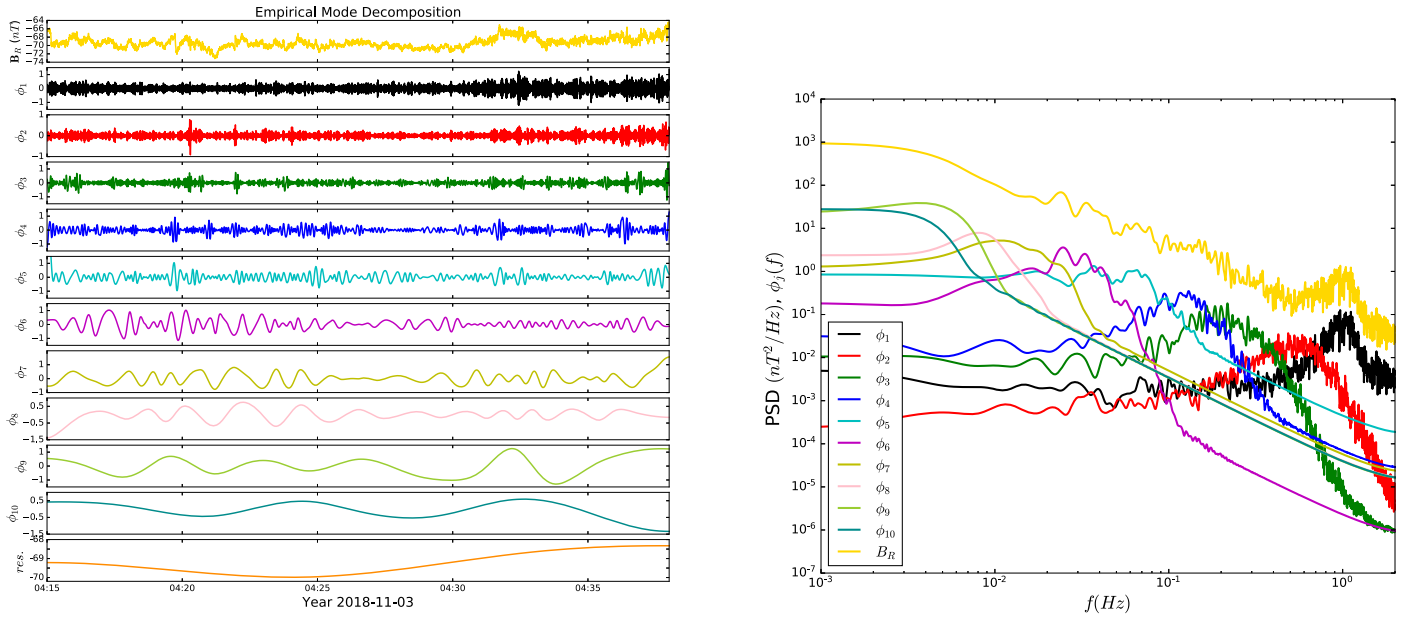

Figure 4. Left panel shows the various IMFs ϕ_i ($i = 1, 2, \ldots, 10$) and the residual trend from the EMD procedure for the B_R component during the selected interval in Figure 1. Right panel shows the Fourier PSD as a function of frequency. The yellow curve represents the PSD of the original signal of B_R and the others represent the individual PSDs of ten different IMFs ϕ_1, ϕ_2, …, ϕ_{10}.

in which PV indicates the principal value of the singular integral, $A_j(t) = \sqrt{\phi_j^2 + \tilde{\phi}_j^2}$ is the instantaneous amplitude, and $\theta_j(t) = \arctan\left(\frac{\tilde{\phi}_j}{\phi_j}\right)$ is the phase function. The instantaneous frequency can then be calculated by the time derivative of $\theta_j(t)$, i.e.,

$$\omega_j(t) = \frac{d\theta_j}{dt}.$$

Therefore, a total of k of the IMFs $\phi_j(t)$, $j = 1, 2, \ldots, k$ with the analytic signals $Z_j(t)$ correspond to k instantaneous amplitudes $A_j(t)$ and frequencies $\omega_j(t)$. Although the instantaneous amplitude depends on time only, we may treat it as a function of both the instantaneous frequency and time $A_j(t) = A(\omega_j(t), t)$. This frequency-time distribution of the amplitude is defined as the Hilbert spectrum $H(\omega, t) \equiv A(\omega, t)$. The square of the Hilbert spectrum divided by frequency $H^2(\omega, t)/\omega$ corresponds to the usual spectral density.

The Hilbert spectrum is similar to the wavelet spectrogram (e.g., Zhao et al. 2020) in the sense that both are functions of time and frequency. The major difference is that the wavelet bases are preselected, while the HSA is adaptive to the data. Since the Hilbert spectrum is expressed in the instantaneous frequency, there is no limit on the frequency resolution.

3. Results

Two intervals, listed in Table 1, that satisfy our criteria are selected from 20 days of data that have high-resolution (∼0.22s) plasma data (2018 November 1–10 and 2019 April 1–10. Each of the two intervals is located in a slow solar wind region with relatively low magnetic fluctuations. Some characteristic parameters related to each interval are listed as well.

As an example, we present a complete analysis of the first interval. Results from the second interval exhibit similar spectral properties to the first so we do not present the full analysis to avoid redundancy. The magnetic power spectra for the second interval are shown at the end of this section. Figure 1 displays a 5 hr time-series plot of the varying flow speed and magnetic field components from 2018 November 3 02:00 UT to 2018 November 3 07:00 UT measured by the PSP/SWEAP and PSP/FIELDS instruments. Both the magnetic field and flow speed have a cadence of ∼0.22 s. Panels from top to bottom display the time evolution of the three components of the solar wind speed V_R, V_T, and V_N, magnetic field components B_R, B_T, and B_N, and the angle θ_{VB} between magnetic field and flow speed vectors. Although the flow near perihelion is in the slow solar wind region, the magnetic field and flow velocity vectors are correlated on average, consistent with a generally Alfvénic flow. However, due to the prevailing spikes caused by magnetic switchbacks or other subtle structures, the time profile of angle θ_{VB} jumps up and down, ensuring that criterion (i) is not easily satisfied. The interval dated from 04:15:35 to 04:38:36 UT on 2018 November 3 is selected and is the pink shaded area in each panel of Figure 1. This interval possesses the strict field-aligned characteristics of our criteria. Some parameters in this interval are summarized in Table 1.

The magnetic compressibility of this interval can be seen from Figure 2, where the standard Fourier power spectral densities (PSD) of the three magnetic field components B_R, B_T, and B_N are shown in the left panel. The PSD of a signal $x(t)$ is calculated by the Fourier transform of the autocorrelation function of the signal (e.g., Leamon et al. 1998; Zhao et al. 2019): $P(x) = \mathcal{F}(\langle x(\tau)x(\tau + t)\rangle)$. A Kolmogorov $f^{-5/3}$ spectrum is displayed for reference. The proton gyrofrequency f_p is calculated using the mean magnetic field in the interval. We find all three magnetic field components exhibit a Kolmogorov-like $f^{-5/3}$ spectrum. The fluctuations are contained mostly in the T and N components, which suggests primarily nearly incompressible fluctuations in the interval since the mean magnetic field is approximately along the

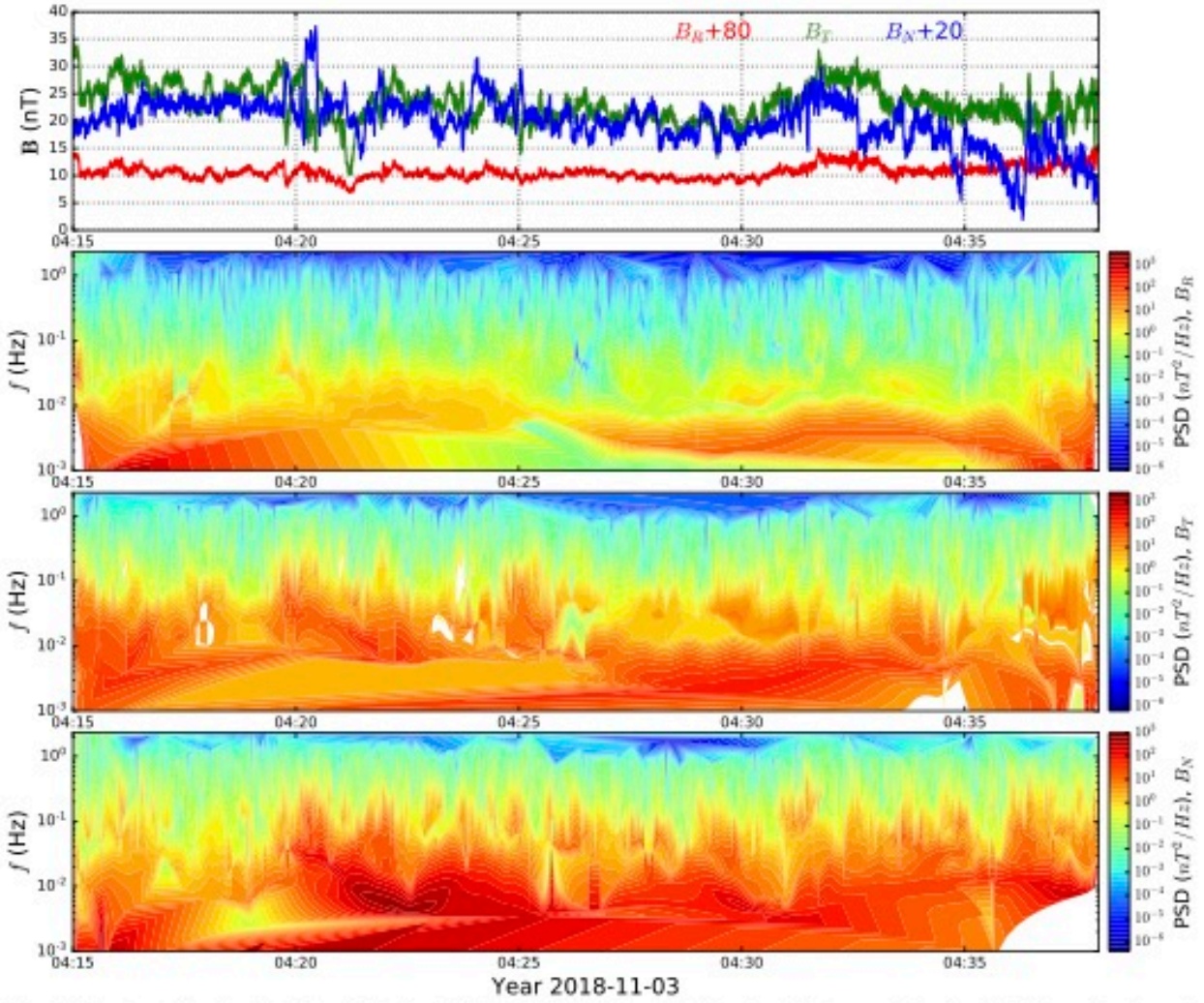

Figure 5. Hilbert spectra for the selected interval dated from 04:15:35 to 04:38:36 UT on 2018 November 3. The top panel shows the shifted time series of magnetic field components B_R, B_T, and B_N. The bottom three panels show contour plots of the Hilbert power spectrograms of B_R, B_T, and B_N as a function of time and frequency.

R direction. This can be further seen from the right panel of Figure 2, which shows the frequency-dependent magnetic compressibility, defined as $C_B = \frac{P(|B|)}{P(B_R)+P(B_T)+P(B_N)}$, where the numerator represents the power in the magnetic field amplitude fluctuations and the denominator represents the total power in the magnetic field fluctuations. Note that there is an enhancement of wave power near the proton gyrofrequency f_p, which is consistent with PSP observations in the quiet solar wind conditions (Bale et al. 2019) and indicates a transition from large MHD inertial range turbulence to kinetic range turbulence. This further confirms that the interval we selected does not contain switchback or magnetic jet structures. The magnetic compressibility increases at high frequencies, as expected for kinetic range turbulence, but remains at a relatively low value (less than 0.2), thus suggesting the Alfvénic nature of the fluctuations.

To further understand the nature of the fluctuations, we have also evaluated the Fourier spectra of the normalized cross helicity σ_c and normalized residual energy σ_r. The normalized cross helicity $\sigma_c = 2\langle \boldsymbol{u}\cdot\boldsymbol{b}\rangle/(\langle u^2\rangle + \langle b^2\rangle)$ and normalized residual energy $\sigma_r = (\langle u^2\rangle - \langle b^2\rangle)/(\langle u^2\rangle + \langle b^2\rangle)$ are calculated from the fluctuating velocity field $\boldsymbol{u}$ and fluctuating magnetic field $\boldsymbol{b}$ (expressed in Alfvén units). The magnitudes of σ_c and σ_r are often used to quantify the Alfvénicity of solar wind turbulence. Unidirectional Alfvén waves usually have a typical $|\sigma_c|$ close to 1 and σ_r close to zero. In the left panel of Figure 3, we show the Fourier power spectra of σ_c and σ_r for the interval selected in Figure 1. The right panel shows the trace power spectrum (black curve) of the velocity fluctuations and the spectrum of the velocity magnitude fluctuations (red curve). The trace power spectrum is calculated as the sum of the spectra of three velocity components, which is an order of magnitude larger than the velocity amplitude spectrum. The blue vertical dashed lines in both panels identifies the frequency at which the velocity spectrum starts to flatten and noise becomes important (Parashar et al. 2020; Vech et al. 2020). For the ~5 Hz cadence plasma

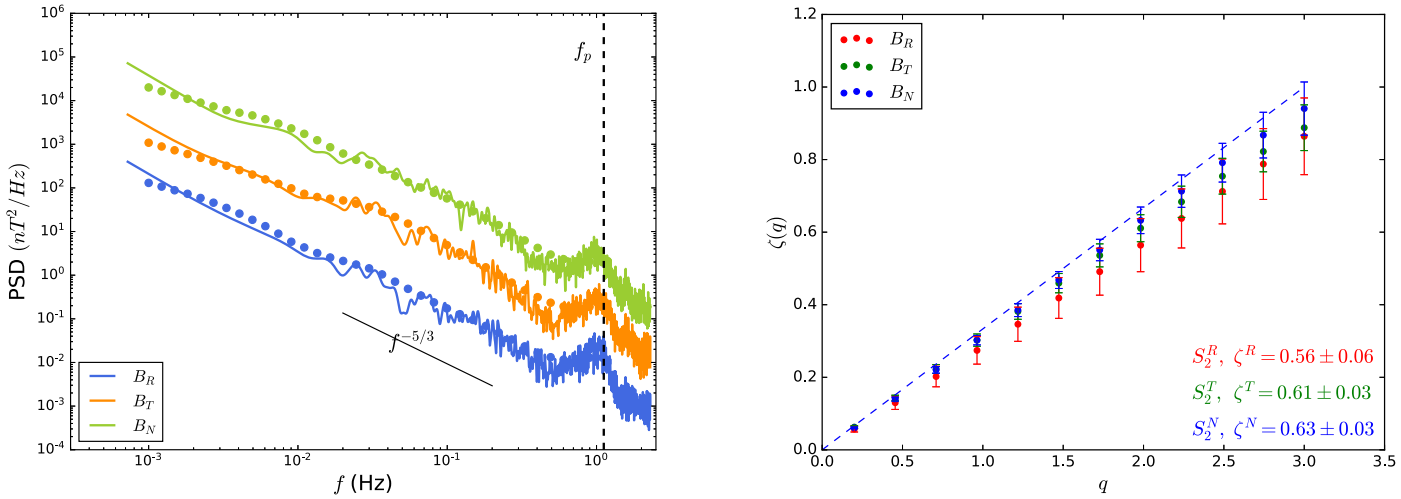

Figure 6. Left panel shows a comparison of the Fourier power spectra (solid curves) and the Hilbert marginal spectra (solid circles) for three magnetic field components during the same interval in Figure 1. The dashed vertical line identifies the proton gyrofrequency. A Kolmogorov-like $f^{-5/3}$ power-law spectrum is displayed for reference. The right panel shows the relation between power-law indices $\zeta(q)$ in the structure functions and the order q of the structure function for B_R, B_T, and B_N respectively. The power-law exponents of the second-order structure functions of each component are listed.

velocity data, the noise floor is around 0.06 Hz (Parashar et al. 2020). In the MHD inertial range down to the noise floor, the velocity fluctuation spectrum basically follows $f^{-1.5}$, and the normalized cross helicity σ_c and residual energy σ_r stay fairly constant with $\sigma_c \simeq 0.8$ and $\sigma_r \simeq 0$. The magnitude of σ_c usually indicates the alignment between magnetic and velocity fluctuations, and σ_r represents the energy difference between them. It is evident that the residual energy σ_r shows a monotonic reduction in magnetic fluctuation dominance as smaller scales, i.e., kinetic scales, are approached. That $\sigma_c \sim 1$ and $\sigma_r \sim 0$ in the inertial range confirms that the selected field-aligned interval is dominated by unidirectional Alfvénic fluctuations.

Besides the standard Fourier analysis, we also perform an HSA on the magnetic field fluctuations in the selected intervals. The principal advantage of HSA is that the basis functions are derived from the signal itself. In contrast to traditional decomposition methods where the basis functions are fixed, the EMD is adaptive and not restricted to stationary data. The data set may be analyzed without introducing spurious harmonics or artifacts near sharp data transitions, which could appear when using classical Fourier filtering or high-order moments analysis. As described in Section 2.2, the process of developing time and frequency-dependent power spectra using HHTs consist of three steps. We first need to decompose each magnetic field component into its IMFs. An example of the EMD for the B_R component is shown in the left panel of Figure 4. During the EMD procedure, a total of 10 IMFs ϕ_1, ϕ_2, …, ϕ_{10} and a residual trend *res*. are obtained for the B_R component. The original signal B_R is equal to the sum of these 10 IMFs and the residual trend *res*. The IMFs are narrow-banded signals in certain frequency ranges. The first IMF ϕ_1 captures the smallest local variation of the signal and corresponds to the highest frequency. Once ϕ_1 is found, it is subtracted from the signal, leaving a smoother residual with a lower frequency. The process then restarted with the residual to obtain a next IMF until there are no maxima or minima in the residual. The last IMF ϕ_{10} corresponds to the lowest frequency signal and is the smoothest compared to the other IMFs. This is illustrated in the right panel of Figure 4, where we perform the standard Fourier spectral analysis on each IMF of the B_R component. The yellow curve represents the PSD of the original signal B_R and the other curves represent the individual PSD of ten different IMFs $\phi_1, \ldots, \phi_{10}$. The superposition of these IMF spectra yields the power spectrum of B_R. The figure shows that each IMF has its peak power at a different frequency range with ϕ_1 corresponding to the highest frequency and ϕ_{10} the lowest. Modes $\phi_i(t)$ $(2 \leqslant i \leqslant 8)$ lie in the inertial range, and the first IMF ϕ_1 (black curve) captures the small-scale dynamics. Large-scale modes $\phi_9(t)$ and $\phi_{10}(t)$ are associated with the energy injection range in the turbulent cascade. The EMD procedure allows us to remove these small-scale and large-scale contributions from spectra in the inertial range.

After the IMFs are determined, the second step consists of calculating the Hilbert transform $\mathcal{H}$ for each IMF mode and the corresponding analytic signal $Z(t)$. Figure 5 shows the results of the HSA on the same interval. The top panel shows the shifted time evolution of three magnetic field components B_R, B_T, and B_N. The bottom three panels show contour plots of the Hilbert spectrograms $H^2(\omega, t)/\omega$ of B_R, B_T, and B_N as a function of time and frequency. Unlike the Fourier or wavelet method that has a preselected frequency range, the frequency range in the Hilbert spectrogram is data adaptive and time dependent. In Figure 5, we set the minimum frequency to 10^{-3} Hz when plotting. Note that the minimum frequency of the spectrogram may be larger than 10^{-3} Hz, which can be seen at the bottom-right corner of the B_N panel and the bottom-left corner of the B_R panel. The spectrograms show clearly that (i) the magnetic fluctuation power decreases with increasing frequency at all time as expected; (ii) for a given frequency, the fluctuations along the B_T and B_N directions are larger than in the B_R component, and the fluctuation intensity is slightly greater in the B_N component than in the B_T component; (iii) a modulation in the amplitude of the maximum power is notable for the B_T and B_N components at around 10^{-1} Hz, and the B_R component varies relatively smoothly from low to high frequencies, which may be due to the inherent fluctuations in B_T and B_N. To summarize, the dominant fluctuation energy during this interval resides in the transverse directions, which is consistent with the Fourier power spectrum shown in Figure 2. The spectrograms suggest

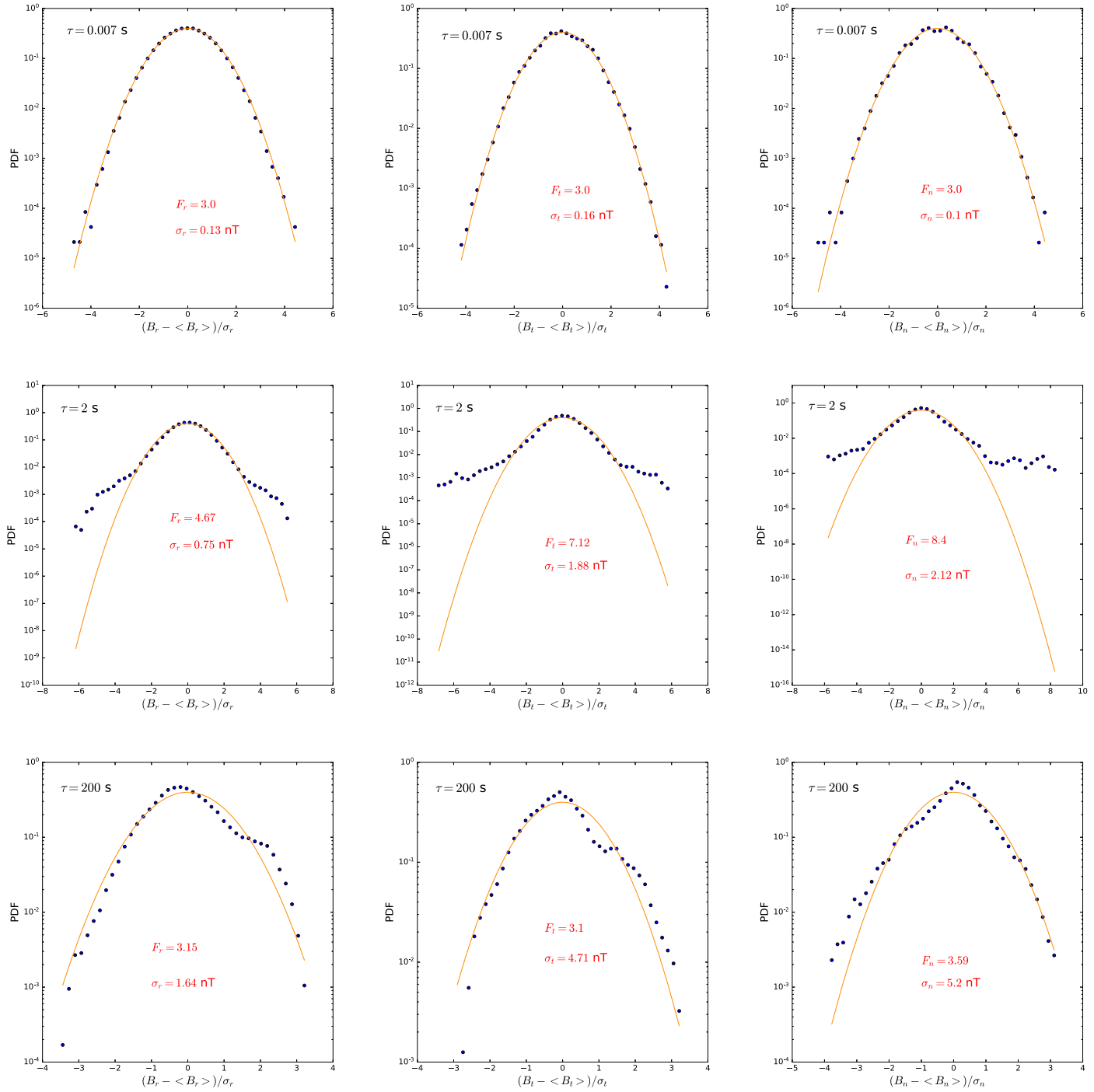

Figure 7. The pdfs of the B_r, B_t, and B_n components at three different time lags: 0.007 s (top row), 2 s (middle row), and 200 s (bottom row). The Gaussian distribution is displayed as a reference. The flatness F and standard deviation σ for B_R, B_T and B_N are listed in the figure. The timescale $\tau = 200$ s lies in the inertial range, $\tau = 2$ s is within the kinetic range, and $\tau = 0.007$ s is in the instrument noise floor.

that the fluctuations of all three magnetic field components do not exhibit rapid variations, thus indicating that the analyzed period is fairly quiet.

For convenience, the third step is to integrate the Hilbert spectrum $H(\omega, t)$ over time to obtain the marginal spectrum $h(\omega) = \int_0^T H(\omega, t)dt$, which represents the energy of the signal and can be compared with the standard Fourier spectrum. To perform the integration, we first preselect a range of fixed frequencies and interpolate the Hilbert spectrum onto these frequencies at each time. Then we can simply average the Hilbert spectrum over time to get the marginal spectrum. The left panel of Figure 6 compares the standard Fourier power spectra (curves) and the Hilbert marginal spectra (dots) for B_R, B_T and B_N for the same interval in Figure 5. Both Fourier and Hilbert spectra for the B_N component are multiplied by a factor of 10, and the B_R component is divided by a factor of 3 for presentation purposes. A Kolmogorov power-law spectrum with an index of $-5/3$ is displayed for reference. The spectra of the three magnetic field components calculated by both methods follows a power-law shape and are consistent with

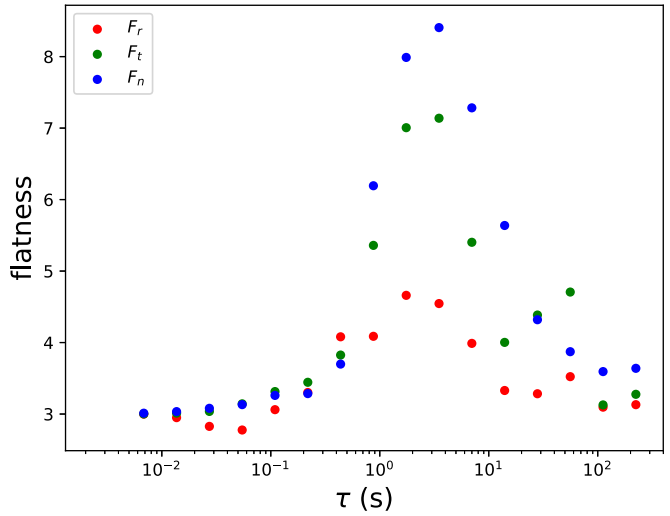

Figure 8. Dependence of the flatness of pdfs on the timescale τ. The B_r, B_t, and B_n components are plotted as red, green, and blue dots, respectively.

each other. For this $k_{\parallel}$ fluctuation interval, a power-law fit in the frequency range $0.01\,\mathrm{Hz} \leqslant f \leqslant 0.5\,\mathrm{Hz}$ gives the spectral exponent of the B_R component as $\sim -1.55 \pm 0.02$, the B_T component as $\sim -1.60 \pm 0.05$, and the B_N component $\sim -1.64 \pm 0.02$. The spectral indices of the three components are far from the "critical balance" theory prediction of f^{-2} for $k_{\parallel}$ fluctuations. In the right panel of Figure 6, we use the structure function method to diagnose the possible influence of intermittency in the interval. The qth-order structure function is defined as $S_q(\tau) = \langle |x(t+\tau) - x(t)|^q \rangle$ for the time-series signal $x(t)$. The Kolmogorov phenomenological theory suggests that the structure function follows a power law with the inertial range time lag τ, i.e., $S_q(\tau) \sim \tau^{\zeta(q)}$. In the absence of intermittency, the power-law index depends linearly on the order of structure function $\zeta(q) = q/3$ (blue dashed line). However, this is rarely observed in experiments due to the presence of intermittency, especially for order $q > 3$. The maximum order $q_{\max}$ can be estimated with a given number N of data points (Dudok de Wit 2004). The empirical criterion $\log(N) - 1$ is usually used to evaluate $q_{\max}$. Structure functions of order larger than $q_{\max}$ cannot be determined accurately (Bruno & Carbone 2013). We calculate the structure functions of various orders up to 3 and perform a power-law fitting to each of them. This is not equivalent to directly fitting the fluctuating power spectrum, which corresponds only to the second-order structure function. We have chosen the range of time lag τ over which the structure functions exhibit a power-law shape. The relation between the power-law indices $\zeta(q)$ and the order of the structure function q for B_R (red dots), B_T (green dots), and B_N (blue dots) in the selected interval are shown in the figure. For a stationary signal, the Fourier power spectrum $P(f) \sim f^{-\alpha}$ corresponds to a power law in the second-order structure function $S_2(\tau) \sim \tau^{\alpha-1}$. As shown in the figure, if $q = 2$, the second-order structure function would satisfy $S_2(\tau) \sim \tau^{0.56\pm0.06}$ for the B_R component, $\tau^{0.61\pm0.03}$ for the B_T component, and $\tau^{0.63\pm0.03}$ for the B_N component. The spectral indices for all three components obtained by using the structure function method ($\alpha_r^s \sim -1.56 \pm 0.06$ for B_R, $\alpha_t^s \sim -1.61 \pm 0.03$ for B_T, and $\alpha_t^s \sim -1.61 \pm 0.03$ for B_N) are approximately consistent with the Fourier power spectrum and Hilbert marginal spectrum.

Besides the structure function method, the distribution of the time series of the magnetic field components can also be used as a indicator of the intermittency. Intermittent structures are often found to possess non-Gaussian distributions. Figure 7 plots the probability density function (pdf) constructed from the time series of the three magnetic field components (B_R, B_T, and B_N) with the resolution of $\sim$0.007 s. The horizontal axis has been normalized by the standard deviation. The solid curve illustrates the standard Gaussian distribution as a reference. We have chosen three different time lags of the magnetic field increments to compute the pdfs at different timescales. The top row shows the pdfs at the smallest timescale of 0.007 s, which corresponds to the smallest time lag, i.e., the resolution of the data. The pdfs for all three components at this timescale follow the Gaussian distribution very well. We have also listed the flatness of the distributions, defined as $F = \langle (x-\bar{x})^4 \rangle / \langle (x-\bar{x})^2 \rangle^2$, for each magnetic field component in the figure. The standard Gaussian distribution has a flatness of $F = 3$. The flatness at the smallest timescale is 3 for all three components, which is caused by the instrument noise. The middle row plots the pdfs at an intermediate timescale of $\sim$2 s, which corresponds to the approach of the kinetic scale. Clear tail distributions are exhibited showing the deviation from the Gaussian distribution. The flatness is 4.67 for B_R, 7.12 for B_T, and 8.4 for B_N. This is a signature of strong intermittent events (Wang et al. 2014). The bottom row shows the pdfs at the timescale of 200 s, corresponding to the inertial range scale. Comparing to the kinetic scale (middle row), the pdfs are closer to Gaussian at the larger inertial range scale and the tails are less pronounced. The flatness for three components are $F_r = 3.15$, $F_t = 3.1$, and $F_n = 3.59$, all close to 3 in this case.

Figure 8 shows the dependence of the flatness of pdfs on the timescale τ. For timescale $\tau \gtrsim 3$ s or frequency $f \lesssim 0.33$ Hz, the flatness decreases with the increase of timescale or the decrease of frequency scale. At timescales larger than $\sim$50 s, the flatness is close to 3, suggesting that the intermittency is small in the inertial range, with which we are mostly concerned. The relatively large flatness for B_N in the inertial range indicates that there may be some intermittent structures in the B_N component. As shown in Figure 5, there are some obvious ramp-cliff structures (e.g., around 4:20) in B_n field. These structures are customary in traditional passive scalar turbulence, and usually affect the scaling exponents resulting in a higher level of intermittency (Bruno et al. 2007; Iyer et al. 2018). For the intermediate timescale region $0.6 \leqslant \tau \leqslant 3$, the flatness for all three components increase, and PDFs deviate from normal distribution, which is due to the approach of the small kinetic scales. At even smaller timescales (much higher frequency scales), the flatness decreases and is close to 3 again. This is probably due to instrumental noise that is approximately Gaussian distribution.

For completeness, the left panel of Figure 9 shows the Fourier power spectra (curves) and the Hilbert marginal spectra (dots) of B_R, B_T, and B_N during the second interval listed in Table 1. Similar to Figure 6, the spectra of each magnetic field component calculated by both methods are consistent with each other. For this interval, a power-law fitting in the inertial range gives the spectral index of the B_R component as $\sim -1.62 \pm 0.03$, the B_T component as $\sim -1.65 \pm 0.02$, and the B_N component as $\sim -1.57 \pm 0.03$. The right panel shows the comparison between the scaling exponents $\zeta(q)$ of the qth-order structure function and the theoretical scaling exponent $q/3$ (in

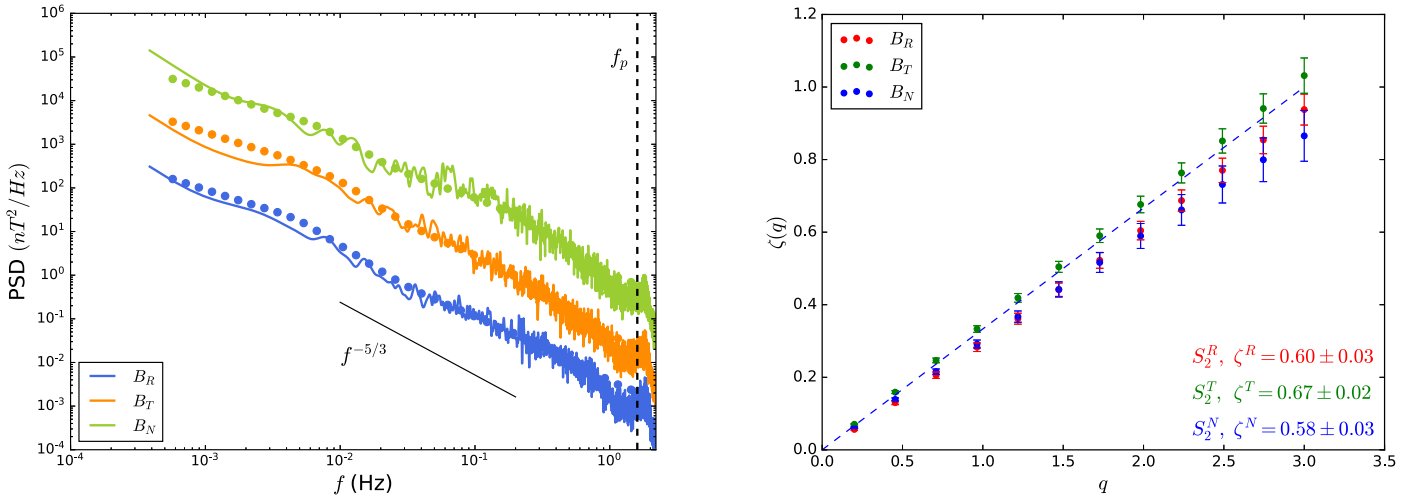

Figure 9. Same as for Figure 6, but for the second interval in Table 1. The spectra in the left panel have been shifted for presentation purpose.

the absence of intermittency) for each magnetic field component. As shown in the right panel, $\zeta(q)$ (dots with error bar) of the three components are basically aligned with $q/3$ (blue dashed line), indicating weak intermittency in this interval. The scaling exponents of the second-order structure functions for three components are listed in the figure, i.e., $S_2^R(\tau) \sim \tau^{0.6\pm0.03}$, $S_2^T(\tau) \sim \tau^{0.67\pm0.02}$, and $S_2^N(\tau) \sim \tau^{0.58\pm0.03}$. The spectral indices inferred from the second-order structure functions (-1.6 ± 0.03 for the B_R component, -1.67 ± 0.02 for the B_T component, and -1.58 ± 0.03 for the B_N component) are basically consistent with those obtained by directly fitting the fluctuating power spectrum.

4. Conclusions

In this paper, we investigated turbulent fluctuations in the field-aligned solar wind flow using PSP data. We performed a systematic search based on the angle between the solar wind flow velocity and magnetic field θ_{VB}. Due primarily to the presence of frequent magnetic switchbacks, field-aligned events are rare. We note that the relative amplitude of magnetic fluctuations in our event are on the order of $|\delta \boldsymbol{B}|/|\boldsymbol{B}_0| \simeq 0.2$. In this case, a rigorous parallel fluctuation should satisfy the condition $\theta_{VB} < \arctan(|\delta \boldsymbol{B}|/|\boldsymbol{B}_0|) \sim 11°$. Although our event selection criterion is $\theta_{VB} \leqslant 20°$, the average angle between field and flow is within 9° during both selected events. Therefore, the two identified events satisfy the parallel fluctuation condition reasonably well. Because of the presence of numerous magnetic switchbacks, a longer interval with parallel fluctuations is not available. However, we caution that although we are sampling with the magnetic field almost aligned to the solar wind vector, a small contamination by perpendicular fluctuations cannot be excluded a priori. Observations at 1 au suggest that Alfvénic fluctuations are most common in fast solar wind streams. By contrast, the two intervals we identified within 0.2 au are associated with the slow solar wind.

Different spectral analysis techniques are applied to the identified events, including the standard Fourier spectrum, Hilbert spectrum, and structure function. For both events, spectral analysis suggests a Kolmogorov-like $f^{-5/3}$ power law for the magnetic field power spectra. The critical balance theory of Goldreich & Sridhar (1995) predicts a $k_\parallel^{-2}$ parallel power-law spectrum. Previous 1 au observational studies of the solar wind have reported contradicting results regarding the spectrum, with both $k_\parallel^{-2}$ and $k_\parallel^{-5/3}$ spectra apparently observed (e.g., Horbury et al. 2008; Telloni et al. 2019). Our analysis provides further evidence closer to the Sun that the spectrum for what appears to be unidirectionally propagating Alfvén waves is $k_\parallel^{-5/3}$. This is inconsistent with both critical balance and weak MHD turbulence theory. It should be noted that the critical balance theory provided by Goldreich & Sridhar (1995) requires counter-propagating Alfvén waves, i.e., cross helicity $\sigma_c \sim 0$, while we find unidirectional Alfvénic fluctuations ($\sigma_c \sim 1$) in both events. However, Lithwick et al. (2007) extended the critical balance conjecture to include imbalanced turbulence. The results presented here are therefore not consistent with the critical balance predictions.

We also quantified the level of intermittency in the observed events as previous studies suggest that the presence of intermittent structures can strongly affect the turbulence power spectrum (e.g., Li et al. 2011; Wang et al. 2014). The scaling exponents of the qth-order structure functions of the three magnetic field components in both intervals are compatible with the theoretical scaling exponents $q/3$ (which holds in the absence of intermittency). In addition, probability distributions constructed from the magnetic field difference show that the pdfs are approximately Gaussian in the inertial range and no clear tail was found. All of these characteristics indicate that intermittency is weak in the selected intervals. By examining the level of intermittency, we stress that the $-5/3$ scaling index in the interval is not caused by current sheets and other intermittent structures, but instead is the intrinsic spectral index of $k_\parallel$ fluctuations.

Finally, we point out that a possible explanation of the observed $k_\parallel^{-5/3}$ spectrum in unidirectional Alfvénic fluctuations emerges from the NI MHD theory. Zank et al. (2017) show that the perpendicular power spectrum follows a $k_\perp^{-5/3}$ power law, which is the same as the critical balance prediction, but is due to 2D structures instead of the interaction of Alfvén waves. The parallel power spectrum is given by the NI corrections to the core 2D MHD equations. For highly imbalanced turbulence ($|\sigma_c| \sim 1$), the NI MHD theory admits a Kolmogorov-like $k_\parallel^{-5/3}$ inertial range spectrum. From an observational perspective, we note that Wang et al. (2015)

found a $k_{\parallel}^{-5/3}$ scaling for weak turbulent fluctuations, which seems to be the case in our study. For moderate-amplitude fluctuations of $|\delta \boldsymbol{B}|/|\boldsymbol{B}_0| \simeq 0.4$, they found a $k_{\parallel}^{-2}$ scaling, which is consistent with critical balance theory. However, Telloni et al. (2019) found that parallel fluctuations exhibit a $-5/3$ scaling even in the strong turbulence regime with $|\delta \boldsymbol{B}|/|\boldsymbol{B}_0| \geqslant 0.3$–$0.4$. In the companion paper of Adhikari et al. (2020), the exact spectral shape does not depend on the amplitude of the fluctuations, but the relation between the transition wavenumber k_t (defined in Zank et al. 2020), perpendicular wavenumber $k_{\perp}$, and parallel wavenumber $k_{\parallel}$. In their study, the parallel fluctuation spectra satisfy a -2 scaling only when $k_{\perp} k_t^{1/2} = k_{\parallel}^{3/2}$. A detailed theoretical study on the nature of solar wind turbulence anisotropy is presented in Zank et al. (2020), which focuses on the turbulence power spectra of different forms in the framework of the NI MHD theory.

We acknowledge the partial support of an NSF EPSCoR RII-Track-1 Cooperative Agreement OIA-1655280, and partial support from an NSF/DOE Partnership in Basic Plasma Science and Engineering via NSF grant PHY-1707247, and a NASA Parker Solar Probe contract SV4-84017. We thank the NASA Parker Solar Probe SWEAP team led by J. Kasper and FIELDS team led by S. D. Bale for use of data. D.T. was partially supported by the Italian Space Agency (ASI) under contract I/013/12/0. F.C. was partially supported by the ERA-PLANET program (www.era-planet.eu) (Contract.no. 689443) within the IGOSP project (www.igosp.eu).

ORCID iDs

L.-L. Zhao https://orcid.org/0000-0002-4299-0490
G. P. Zank https://orcid.org/0000-0002-4642-6192
L. Adhikari https://orcid.org/0000-0003-1549-5256
D. Telloni https://orcid.org/0000-0002-6710-8142
F. Carbone https://orcid.org/0000-0002-3559-5273

References

Adhikari, L., Zank, G. P., Hunana, P., et al. 2017, ApJ, 841, 85
Adhikari, L., Zank, G. P., & Zhao, L.-L. 2019, ApJ, 876, 26
Adhikari, L., Zank, G. P., Zhao, L. L., et al. 2020, ApJ, submitted
Bale, S. D., Badman, S. T., Bonnell, J. W., et al. 2019, Natur, 576, 237
Bale, S. D., Goetz, K., Harvey, P. R., et al. 2016, SSRv, 204, 49
Bavassano, B., Dobrowolny, M., Fanfoni, G., et al. 1982, SoPh, 78, 373
Bieber, J. W., Wanner, W., & Matthaeus, W. H. 1996, JGR, 101, 2511
Bruno, R., & Carbone, V. 2013, LRSP, 10, 2
Bruno, R., Carbone, V., Chapman, S., et al. 2007, PhPl, 14, 032901
Carbone, F., Sorriso-Valvo, L., Alberti, T., et al. 2018, ApJ, 859, 27
Chen, C. H. K., Mallet, A., Yousef, T. A., et al. 2011, MNRAS, 415, 3219
Dasso, S., Milano, L. J., Matthaeus, W. H., et al. 2005, ApJL, 635, L181
Dudok de Wit, T. 2004, PhRvE, 70, 055302
Dudok de Wit, T., Krasnoselskikh, V. V., Bale, S. D., et al. 2020, ApJS, 246, 39
Fox, N. J., Velli, M. C., Bale, S. D., et al. 2016, SSRv, 204, 7
Fu, S., Zhao, L., Zank, G. P., et al. 2020, SCPMA, 63, 219511
Goldreich, P., & Sridhar, S. 1995, ApJ, 438, 763
Horbury, T. S., Forman, M., & Oughton, S. 2008, PhRvL, 101, 175005
Horbury, T. S., Wicks, R. T., & Chen, C. H. K. 2012, SSRv, 172, 325
Horbury, T. S., Woolley, T., Laker, R., et al. 2020, ApJS, 246, 45
Huang, Y. X., Schmitt, F. G., Hermand, J.-P., et al. 2011, PhRvE, 84, 016208
Huang, Y. X., Schmitt, F. G., Lu, Z. M., et al. 2008, EL, 84, 40010
Hunana, P., & Zank, G. P. 2010, ApJ, 718, 148
Iyer, K. P., Schumacher, J., Sreenivasan, K. R., et al. 2018, PhRvL, 121, 264501
Kasper, J. C., Abiad, R., Austin, G., et al. 2016, SSRv, 204, 131
Kasper, J. C., Bale, S. D., Belcher, J. W., et al. 2019, Natur, 576, 228
Leamon, R. J., Smith, C. W., Ness, N. F., et al. 1998, JGR, 103, 4775
Li, G., Miao, B., Hu, Q., et al. 2011, PhRvL, 106, 125001
Lithwick, Y., Goldreich, P., & Sridhar, S. 2007, ApJ, 655, 269
Matthaeus, W. H., Dasso, S., Weygand, J. M., et al. 2005, PhRvL, 95, 231101
Matthaeus, W. H., Goldstein, M. L., & Roberts, D. A. 1990, JGR, 95, 20673
McManus, M. D., Bowen, T. A., Mallet, A., et al. 2020, ApJS, 246, 67
Milano, L. J., Dasso, S., Matthaeus, W. H., et al. 2004, PhRvL, 93, 155005
Narita, Y., Sahraoui, F., Goldstein, M. L., et al. 2010, JGR, 115, A04101
Parashar, T. N., Goldstein, M. L., Maruca, B. A., et al. 2020, ApJS, 246, 58
Podesta, J. J. 2009, ApJ, 698, 986
Ruiz, M. E., Dasso, S., Matthaeus, W. H., et al. 2011, JGR, 116, A10102
Telloni, D., Carbone, F., Bruno, R., et al. 2019, ApJ, 887, 160
Tessein, J. A., Smith, C. W., MacBride, B. T., et al. 2009, ApJ, 692, 684
Vech, D., Kasper, J. C., Klein, K. G., et al. 2020, ApJS, 246, 52
Wang, X., Tu, C., He, J., et al. 2014, ApJL, 783, L9
Wang, X., Tu, C., He, J., et al. 2015, ApJL, 810, L21
Yang, L., He, J., Tu, C., et al. 2017, ApJ, 846, 49
Zank, G. P., Adhikari, L., Hunana, P., et al. 2017, ApJ, 835, 147
Zank, G. P., & Matthaeus, W. H. 1992, JGR, 97, 17189
Zank, G. P., & Matthaeus, W. H. 1993, PhFl, A5, 257
Zank, G. P., Nakanotani, M., Zhao, L.-L., Adhikari, L., & Telloni, D. 2020, ApJ, submitted
Zhao, L.-L., Adhikari, L., Zank, G. P., et al. 2017, ApJ, 849, 88
Zhao, L. L., Zank, G. P., Adhikari, L., et al. 2020, ApJS, 246, 26
Zhao, L.-L., Zank, G. P., Chen, Y., et al. 2019, ApJ, 872, 4